ACS NANO

www.acsnano.org

From Sequential Molecular Adsorption on Atomically Precise Ag_{29} Nanoclusters to Aggregates of Soot-Like Particles

Jayoti Roy, Marco Neumaier, Christoph Plett, Papri Chakraborty, Anirban Som, Arijit Jana, Stefan Grimme, Horst Hahn, Manfred M. Kappes,* and Thalappil Pradeep*

Cite This: https://doi.org/10.1021/acsnano.6c03086

Read Online

ACCESS | Metrics & More | Article Recommendations | Supporting Information

ABSTRACT: Adsorption of molecules onto the surface of atomically precise, ligand-protected metal nanoclusters (NCs) is a complex and, unlike ligand exchange, relatively unexplored aspect of NC chemistry. It has significant implications for catalysis as well as for particle nucleation and growth, e.g., in the context of atmospheric chemistry. Here, we investigate the solution-phase adsorption of dithiol molecules, 2,2'-[1,4-Phenylenebis(methylidynenitrilo)]bis[benzenethiol], (abbreviated as $R1S_2H_2$) on atomically precise $[Ag_{29}(BDT)_{12}]^{3-}$ NCs (where BDT is 1,3-benzenedithiol). Using electrospray ionization mass spectrometry (ESI MS), high-resolution transmission electron microscopy (HRTEM), and dynamic light scattering (DLS) to probe solution composition after mixing, we resolve rapid adsorption of multiple $R1S_2H_2$ secondary ligands onto individual NCs. This is also associated with the formation of NC dimers (detectable by ESI MS) and eventually larger aggregates. Time-dependent measurements at high mass resolution show increasing hydrogen atom loss from the adsorbate modified NCs (and dimers), indicating a transition from a pure physisorptive to a partially chemisorptive state. Molecular docking simulations and density functional theory calculations were used to elucidate the multilayered, soot-particle-like structures of the NC adducts and to establish binding energies for secondary ligand adsorption which govern their assembly and aggregation. These observations provide valuable insights into the complex supramolecular interactions which can occur within the outer shell of NCs exposed to secondary ligands. The observation of the dynamic interplay between physisorptive and chemisorptive phenomena upon aging of the reaction mixture provides important mechanistic insights into the aggregation and growth of nanoscale particles starting from NCs.

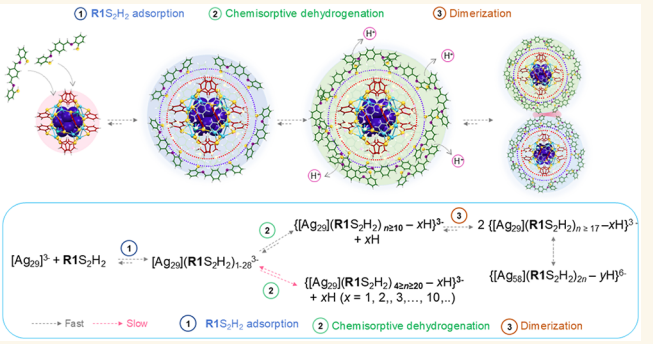

KEYWORDS: *atomically precise noble metal nanoclusters, supramolecular interactions, secondary ligand interaction, dimerization, soot-like particles, assembly*

INTRODUCTION

Organic molecule-protected metal nanoclusters (NCs) exhibit core−shell-like structures, comprising a metal core protected by a monolayer of ligands.[1,2] These ligands are essential for preventing aggregation in solution, imparting stability to the NCs, and tuning their properties.[3−5] Over the past few decades, systematic ligand exchange has imparted new properties to NCs[6−8] and has helped the synthesis of new NCs with well-defined structures.[9−14] Their molecular composition is typically elucidated with mass spectrometry using different ionization methodologies, such as electrospray ionization (ESI) or matrix-assisted laser desorption ionization (MALDI).[1,15−18]

NCs can interact with other NCs, nanoparticles, or molecules through their native surface ligands or through incoming (secondary) ligands that coadsorb on the NC surface. Interactions of various types, such as intercluster interactions,[19−22] metal ion/thiolate interactions,[23−25] isotopic exchange,[25,26] charge−transfer interactions,[27] C−H−π, $\pi-\pi$ interactions,[28,29] etc. of NCs have been investigated.

Received: February 15, 2026
Revised: June 4, 2026
Accepted: June 5, 2026

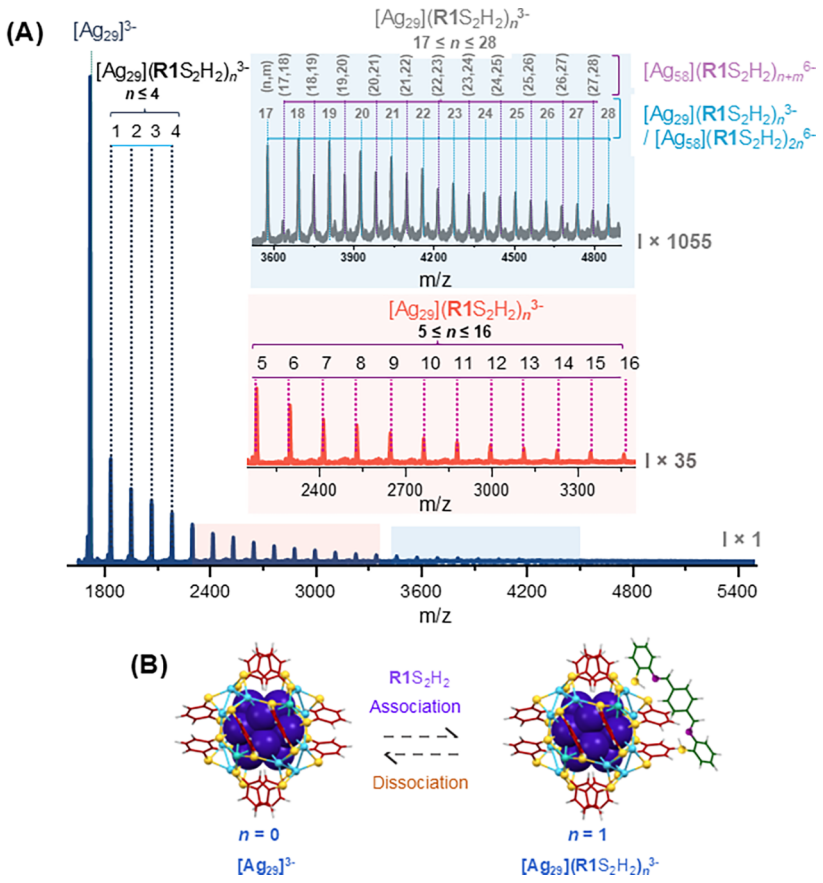

Figure 1. (A) Full range negative ion ESI MS spectrum for a molar ratio of $[Ag_{29}]^{3-}$:$R1S_2H_2$ = 0.14 recorded within 60 s after mixing. The strongest ion peaks associated with $[Ag_{29}]^{3-}$ and $[Ag_{29}](R1S_2H_2)_n^{3-}$ ($1 \le n \le 4$) adduct ions are labeled. The insets show enlarged spectra over the m/z ranges 2100−3500 and 3550−4900, indicating further small- ($1 \le n \le 9$), medium- ($10 \le n \le 16$), and large-sized ($n \ge 17$) monomeric adducts-together with dimers $[Ag_{58}](R1S_2H_2)_{n+m}^{6-}$ ($n + m \ge 34$). Peaks are labeled by the nominal number of attached $R1S_2H_2$ ligands (hydrogen-loss from monomeric adducts and dimers cannot be seen at this scale). (B) Schematic representation of the first (in a sequence of) bimolecular physisorption (association) and unimolecular desorption (dissociation) reactions, shaping the initial composition of the solution.

Furthermore, the precise molecular dimensions and orientation of surface ligands can give rise to distinct noncovalent host−guest interactions.[30−34] A recent study has further shown that ligand functionalization of $[Ag_{29}(S_2R)_{12}]^{3-}$ NCs can direct solvent- and cation-dependent 2D supramolecular assemblies through ligand-mediated coordination interactions.[35]

In a study of intercluster interactions, Nakashima et al. have recently demonstrated that the electrostatic repulsion between dimers of $[M(Au_{24})(SC_nH_{2n+1})_{18}]^-$ NCs (M = Au, Pt; n = 6, 8, 10, 12) in the gas phase is effectively mitigated through the combined influence of aurophilic interactions and van der Waals (vdW) attractions primarily mediated by the ligands.[31] In recent years, several studies on supramolecular chemistry[32] or host−guest interactions between metal NCs and host molecules have been reported,[36−41] in systems including $[Au_{25}(SR)_{18}]^-$,[15] $[Ag_{44}(SR)_{30}]^{4-}$,[42] $[Ag_{29}(S_2R)_{12}]^{3-}$,[43] $[Ag_{25}(SR)_{18}]^-$,[44] and $[Au_{102}(SR)_{44}]^{-/2-}$,[45] where SR and S_2R denote thiol and dithiol ligands, respectively.[20,46−54] However, many NC-based supramolecular structures remain unresolved by X-ray crystallography, leaving key interaction mechanisms unclear.

While bulk metal surfaces like Au(111) have been extensively studied for thiol adsorption,[55−58] surfaces of NCs may exhibit entirely new processes. Thiol adsorption on Au surfaces shows that shorter chains promote surface reconstruction and Au adatom formation.[52−61] Similarly, ligand adsorption or secondary ligand adsorption on NCs can induce structural changes affecting stability, reactivity, and aggregation of the NCs.[62,63] For example, halide ion adsorption on silver NCs can induce defect sites that drive growth and chirality changes.[64] Secondary ligands can also enhance interfacial rigidity and promote self-assembly, as seen in Au_{11} NCs stabilized by phosphine ligands.[65] Engineering the surface environment of silver NCs has also been shown to enhance NC stability and induce unique intercluster packing arrangements within supracrystal lattices.[66]

These studies underscore that secondary molecular interactions with NCs are highly dependent on the ligand shell and staple motifs, owing also to the high surface-to-volume ratios of the NCs. Yet, several aspects remain unresolved: (i) the relative importance of noncovalent interactions (e.g., H-bonding, $\pi\cdots\pi$, C−H$\cdots\pi$, vdW interactions) in solution and gas phase; (ii) the potential transformation of noncovalent to covalent bonding during aggregation; and (iii) the effect of such interactions on the stability of the metal core of the NC-possibly resulting in structural interconversion and finally, (iv) the overall evolution of such complex structures during solution aging.

Recently, we reported the dynamic behavior of ligand-protected $[Ag_{29}(BDT)_{12}]^{3-}$ NCs (BDT = 1,3-benzene-dithiol)

https://doi.org/10.1021/acsnano.6c03086
ACS Nano XXXX, XXX, XXX−XXX

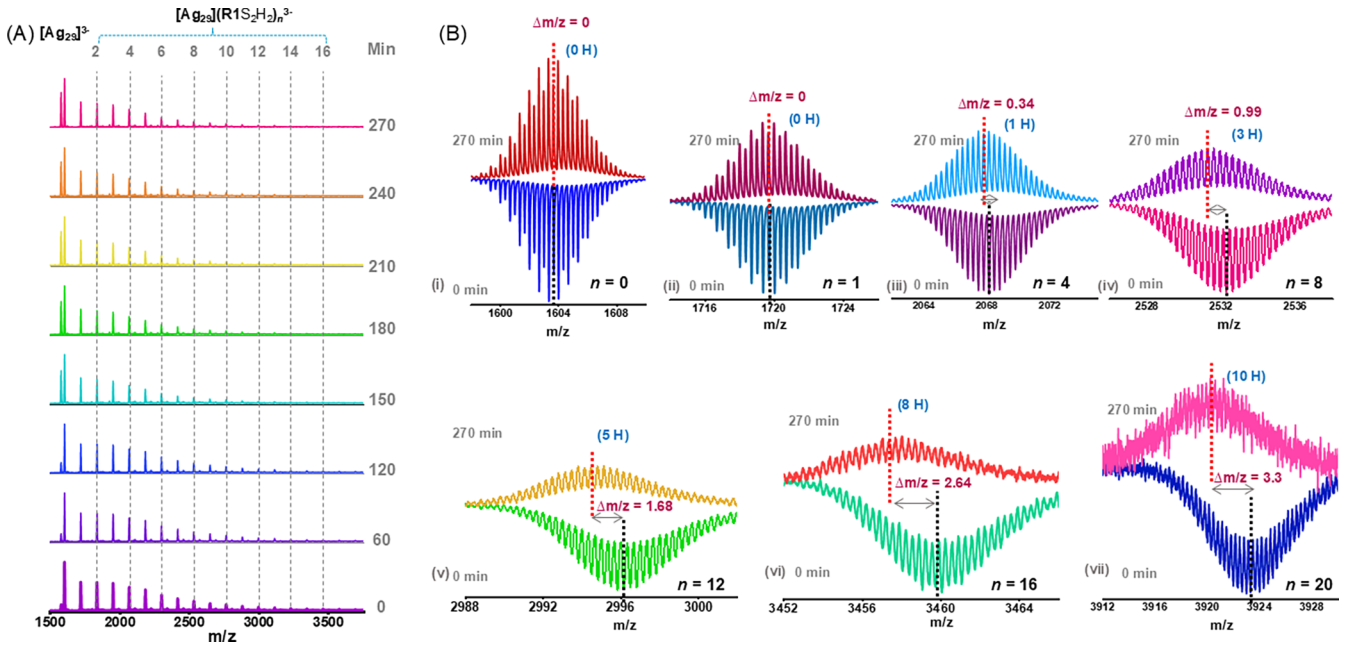

Figure 2. (A) ESI MS taken with a timsTOF versus reaction time in solution, 0−270 min, for a $[Ag_{29}]^{3-}$:R1S$_2$H$_2$ molar ratio of 0.14. *n* indicates the nominal number of attached secondary ligands. (B)(i-vii) Stacked reverse overlay plots at high mass resolution showing positive going $\{[Ag_{29}](R1S_2H_2)_n\text{-}x\text{H}\}^{3-}$ product intensities at 270 min versus negative going intensities at 0 min for *n* = 0, 1, 4, 8, 12, 16, and 20, respectively. Δ*m*/*z* represents the difference in average *m*/*z* between measurements at 0 and 270 min. Note that some H-loss has already occurred at 0 min for *n* ≥ 10 (within 60 s of mixing) as indicated by vertical tic marks (color: dark gray) corresponding to the expected maxima of the isotopologue distributions for purely R1S$_2$H$_2$ physisorption.

interacting with a few molecules of secondary ligand, 2,2'-[1,4-phenylenebis (methylidynenitrilo)]bis[benzenethiol] (referred to as **R1**S$_2$H$_2$).[40] Sequential attachment and detachment of **R1**S$_2$H$_2$ induced structural changes in the NC, affecting its geometry as revealed by ion mobility MS. In this paper, we now investigate the continued adsorption of more molecules of this long-chain dithiol ligand onto $[Ag_{29}(BDT)_{12}(PPh_3)_4]^{3-}$ using ESI-MS, high-resolution transmission electron microscopy (HRTEM), and density functional theory (DFT) calculations to explore particle growth and interparticle interactions in solution. Our results show that increasing the number of adsorbed dithiol ligands drives the formation of supramolecular assemblies via ligand-mediated dimerization. Time-dependent studies also reveal a transition from physisorption to chemisorptive interlinking of individual **R1**S$_2$H$_2$ ligands enhancing structural stability and promoting subsequent aggregation.

These findings highlight the dynamic nature of ligand interactions with NCs, where shifts from noncovalent to covalent bonding can profoundly impact structural integrity and stability—thus demonstrating the potential of ligand design in tailoring NC architectures for diverse applications.

RESULTS/DISCUSSION

Formation of Secondary Ligand Adducts

The NC, $[Ag_{29}(BDT)_{12}(PPh_3)_4]^{3-}$ (BDT and PPh_3 are 1,3-benzene dithiol and triphenylphosphine, respectively) and the secondary dithiol ligand, **R1**S$_2$H$_2$, were synthesized following previous reports.[40,43] The structure of $[Ag_{29}(BDT)_{12}(PPh_3)_4]^{3-}$ features four distinct Ag sites: one central Ag atom in the icosahedral core, 12 Ag atoms forming the icosahedral framework, 12 tetrahedral ^{t}Ag atoms bonded to the sulfur atoms of the BDT ligands, and four under-coordinated crown ^{c}Ag atoms that bind to PPh_3.[40,43]

Electrospray ionization mass spectrometry (ESI MS) was used to probe the solution phase composition. Experiments were performed in the negative ion mode using two different mass spectrometers (a Waters Synapt G2-Si at IIT Madras and a Bruker timsTOF at KIT). Upon ESI MS, the pure NC appeared primarily as $[Ag_{29}(BDT)_{12}]^{3-}$, with a dominant peak at *m*/*z* 1603.[28,67] Experimental and (confirming) theoretical isotopic distributions of this parent ion peak are shown in Supporting Information (Figure S1).

To investigate secondary ligand binding, **R1**S$_2$H$_2$ was added to $[Ag_{29}(BDT)_{12}]^{3-}$ solutions in pure acetonitrile solvent with varying molar ratios. This generated $[Ag_{29}(BDT)_{12}](\mathbf{R1}S_2H_2)_n^{3-}$ and derivatives as detailed below. For simplicity, throughout this work we will abbreviate $[Ag_{29}(BDT)_{12}]^{3-}$ as $[Ag_{29}]^{3-}$ and the $[Ag_{29}(BDT)_{12}](\mathbf{R1}S_2H_2)_n^{3-}$ adducts as $[Ag_{29}](\mathbf{R1}S_2H_2)_n^{3-}$, respectively.

For a typical $[Ag_{29}]^{3-}$:**R1**S$_2$H$_2$ molar ratio of 0.14 (corresponding to a ≈7-fold excess of **R1**S$_2$H$_2$, and a $[Ag_{29}]^{3-}$concentration of $[Ag_{29}]^{3-}$ was ∼50 μM), new peaks appeared in the *m*/*z* range 1700−5400 (Figure 1A), corresponding to adducts $[Ag_{29}](\mathbf{R1}S_2H_2)_n^{3-}$ with *n* ranging from 1 to nominally ≥28 in decreasing intensities. These products form within 60 s of mixing (limited by the transfer time to the mass spectrometer), presumably by sequential association as schematically indicated in Figure 1B. Once formed, there is little further change of adduct intensities for up to 270 min under ambient conditions—indicating a type of adsorption equilibrium is rapidly reached. Surprisingly, the original BDT ligands remain bound to the NC, *indicating that no ligand exchange occurs*. Detailed analysis at higher mass resolution confirmed that **R1**S$_2$H$_2$ initially binds in its intact form, generating adducts such as $[Ag_{29}](\mathbf{R1}S_2H_2)_1^{3-}$ (*m*/*z*

https://doi.org/10.1021/acsnano.6c03086
ACS Nano XXXX, XXX, XXX−XXX

1719), $[Ag_{29}](\mathbf{R1}S_2H_2)_2^{3-}$ (m/z 1835), $[Ag_{29}](\mathbf{R1}S_2H_2)_3^{3-}$ (m/z 1951), $[Ag_{29}](\mathbf{R1}S_2H_2)_4^{3-}$ (m/z 2067), and so on (see Figure 1A). For further discussion below, we will define these species with $0 < n < 10$ as **small-sized** NC ions.

Hydrogen Loss and NC Dimerization

Looking closer, we observe small deviations for $n \geq 10$ between experimentally determined isotopic distributions and those calculated assuming only (intact) $\mathbf{R1}S_2H_2$ physisorption-indicative of the loss of one or more hydrogen atoms. For the discussion below, we will call this "chemisorptive" dehydrogenation. It can already be detected directly after mixing (i.e., within 60 s) independent of ESI settings. Initially limited to loss of about 2H atoms, the extent of dehydrogenation increases with the aging time of the reaction mixture (Figures 2 and S2)—see also next section. We refer to the size range, $10 \leq n \leq 16$, corresponding to NCs that lose measurable numbers of hydrogen atoms within 60 s after mixing but do not form stable gas-phase dimers (shown below) as **medium-sized** NCs. In contrast, the **small-sized** NCs ($n < 10$) of the previous section show only physisorption without any clear hydrogen loss. To more precisely reflect the extent of chemisorptive dehydrogenation, the compositional assignment of these **medium-sized** NCs will from here on be written as$\{[Ag_{29}](\mathbf{R1}S_2H_2)_n - x\mathrm{H}\}^{3-}$ (where x denotes the number of hydrogens lost on average at that particular reaction time and adsorbate coverage n).

From $n \geq 17$, additional peaks spaced by $\Delta m/z = 58$ appear in the mass spectra (also directly after mixing), corresponding to ***6-fold charged dimers*** $\{[Ag_{58}](\mathbf{R1}S_2H_2)_{n+m}\text{-}y\mathrm{H}\}^{6-}$ (y is the average number of hydrogen lost in dimers). These reflect association of two NC monomers having, respectively n and m secondary ligands (see Figures 1A and S3A). Both homodimers ($n = m$) and heterodimers ($n \neq m$) were detected. The size range of NC adducts forming NC dimers detectable by ESI-MS ($n \geq 17$), is defined as **large-sized** NCs. Importantly, parent NC trianions, $[Ag_{29}]^{3-}$, do not form any ESI-MS detectable dimer hexa-anions without addition of $\mathbf{R1}S_2H_2$ to the solution. Expanded scale mass spectra in the range of the **large-sized** NC monomers are shown in Figures 1A and S4. These species also manifest H-loss. However, at high m/z (>3000) the limited mass resolution and broad isotopic distributions complicate quantitative analysis leading to a larger uncertainty in average numbers of H atoms lost. This uncertainty becomes even greater for dimers, due to their lower ion intensity (and smaller isotopologue spacings resulting from the 6- charge). In addition, monomer and dimers signals can overlap, complicating exact MS assignment. For example, the peak labeled with $n = 17$ in Figure 1A (an expanded spectrum is shown in Figure S4) originates from the monomer $\{[Ag_{29}](\mathbf{R1}S_2H_2)_{17} - 4\mathrm{H}\}^{3-}$ and the homodimer $\{[Ag_{58}](\mathbf{R1}S_2H_2)_{34} - 8\mathrm{H}\}^{6-}$, both appearing at $m/z = 3577$. There are also possible contributions from heterodimeric ions $\{[Ag_{58}](\mathbf{R1}S_2H_2)_{n+m} - 8\mathrm{H}\}^{6-}$, where $n + m = 34$, further highlighting the complexity of the MS peak assignment.

Ion intensities of both NC monomers and dimers decreased with increasing secondary ligand number n, likely due to the combined effects of: (i) solution reaction kinetics leading to an early adsorption pre-equilibrium, (ii) fragmentation loss of more weakly bound $\mathbf{R1}S_2H_2$ ligands during ionization or postactivation, (iii) reduced detection efficiency of larger-sized adducts due to increased mass under a constant acceleration potential and/or (iv) selective flocculation/precipitation and thus loss of larger particles from solution upon aging.

Time-Dependent Dehydrogenation

We used ESI timsTOF MS sampling to monitor subtle time-dependent compositional changes to the secondary ligand coverage of NC monomers after mixing $[Ag_{29}]^{3-}$:$\mathbf{R1}S_2H_2$ in a ratio of 0.14—see Figure 2A. For monomers, timesTOF MS offers high mass resolution and sensitivity whereas dimers were not detectable for instrumental reasons.

Figure 2 indicates that for $[Ag_{29}](\mathbf{R1}S_2H_2)_n^{3-}$ with $n = 0-1$, isotopic distributions remain unchanged on a time scale of 270 min, indicating no H loss. However, for $n = 4$, 8, 12, 16, and 20, the apex of the isotopic distribution shifts to lower m/z over time with 1, 3, 5, 8, and 10 H atoms, respectively, lost after 270 min. This highlights slow chemisorptive reactions that continue in solution even hours after mixing. We speculate that H-loss reflects $\mathbf{R1}S_2H_2$ deprotonation via solution redox chemistry involving both NC multianions and adventitious oxidants (such as dissolved O_2). Reaction products (after multiple dehydrogenation) may include: (i) benzothiazoles formed by intramolecular cyclization or (ii) disulfide bridging between secondary ligands of either the same monomer or of two different NCs—in each case with an effective loss of 2H atoms. Note, however, that isotopologue fitting is not precise enough to distinguish between only even H atom loss or a superposition of different processes including loss of an odd number of H atoms.

Mechanistic Interpretation of Ligand Uptake and Dimer Formation

The observed sequential $\mathbf{R1}S_2H_2$ ligand attachment can be rationalized by enhanced metal−ligand interactions and ligand−ligand stabilization within the growing ligand shell. First, $\mathbf{R1}S_2H_2$ possesses increased electron-donating ability toward the crown (c) and tetrahedral (t) Ag sites of the NC due to its electron-rich S and N atoms and extended π-conjugation system. These features strengthen binding to the NC surface, consistent with earlier observations.[40]

Second, incorporation of additional ligands increases the rigidity of the ligand shell, promoted by favorable BDT-BDT, $\mathbf{R1}S_2H_2$-$\mathbf{R1}S_2H_2$, and BDT-$\mathbf{R1}S_2H_2$ ligand interactions. Together, these factors are likely to act synergistically to stabilize the $[Ag_{29}]^{3-}$ NC upon secondary ligand adsorption, effectively encapsulating it within a cage formed by the $\mathbf{R1}S_2H_2$ ligands.

Furthermore, we have noticed that once the number of attached secondary ligands reached 17, the interaction extends beyond the single-cluster level and dimers began to be observed in the mass spectra. We note that the Coulombic repulsion among larger trianionic NCs for $n \geq 17$, diminishes as the number of organic ligands surrounding the NC increases. This reduction in Coulombic repulsion is more pronounced in large-sized NCs compared to their smaller-sized counterparts. For the same reason, while dimers of small- and medium-sized NCs (i.e., $n \leq 16$) may exist in solution, they apparently do not survive electrospray volatilization/ionization presumably because their cohesive interaction (even if disulfide linked via the same physisorbed ligand) is weaker than the Coulomb repulsion. The overall adsorption of $\mathbf{R1}S_2H_2$ ligands onto the $[Ag_{29}]^{3-}$ NC, the subsequent transition from a physisorptive to a chemisorptive state, and the dimerization process are schematically illustrated in Scheme 1.

https://doi.org/10.1021/acsnano.6c03086
ACS Nano XXXX, XXX, XXX−XXX

Scheme 1. Schematic Representation of Sequential Ligand Interaction Processes Observed during Reagent-Ratio- and Time-Dependent ESI MS Analysis of $[Ag_{29}]^{3-}$:R1S$_2$H$_2$-Adducts[a,b]

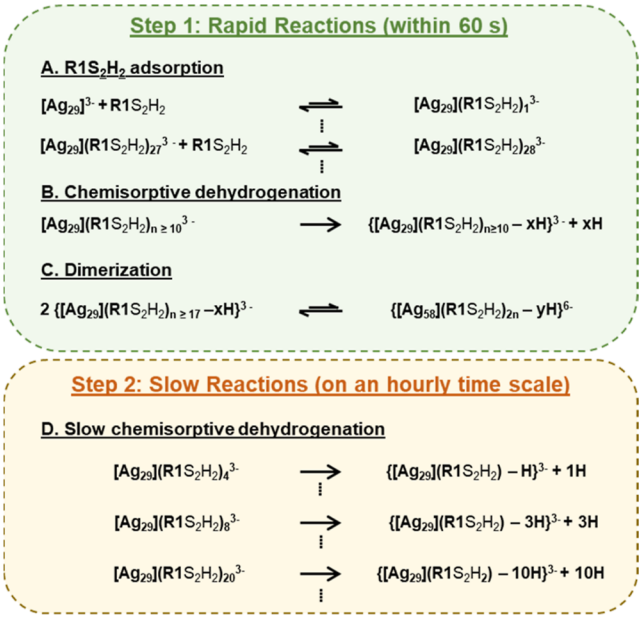

[a]**Step 1** outlines rapid R1S$_2$H$_2$ adsorption and dimerization reactions occurring within 60 s of reagent mixing with no or little H atom loss. [b]**Step 2** illustrates the outcome of solution aging, which is associated with effective H atom loss (possibly as H$_2$) at reaction time >270 min. *x* and *y* denote the number of H atom loss in monomer and dimer, respectively.

Impact of Ligand Concentration on NC Stability

To study the influence of the ligand concentration, we also recorded ESI MS for systematically varied $[Ag_{29}]^{3-}$:R1S$_2$H$_2$ molar ratios between 0.02−0.14 (while keeping the $[Ag_{29}]^{3-}$ concentration constant). Figure 3A presents the corresponding full range ESI MS, while Figure 3B shows an expanded view of the *m*/*z* 2800−4500 range. Note that all MS were recorded within 60 s after preparing solution mixtures with different concentrations of R1S$_2$H$_2$ in a fixed concentration of $[Ag_{29}]^{3-}$ NC. At a molar ratio of 0.14, we see sequential ligand addition to $[Ag_{29}]^{3-}$ and dimer formation of larger-sized NCs (Figure 3A,B(i)) as already discussed above (viz. Figure 1). As the molar ratio is reduced below 0.14 (corresponding to an increase in concentration of the secondary ligand), NC dimer peaks first reduce in intensity and then disappear altogether (Figure 3B). For a 50 fold excess of the ligand ($[Ag_{29}]^{3-}$:R1S$_2$H$_2$ = 0.02), the ESI-MS begin to show distinct NC degradation as indicated by trianionic fragment peaks (Figures 3B(v), and S5) attributable to loss of α—Ag(R1S$_2$H$_2$); β—Ag$_2$(BDT)$_2$; γ—Ag(BDT)$_2$; and δ—Ag(BDT), respectively (Figure S5). Conceivably, this results from interligand reactions possibly catalyzed by electron donation from the NCs (see also discussion of H atom loss above).

Beyond MS: HRTEM and DLS Probes of Aggregation

The ESI-MS platforms used in this study had an effective upper mass detection limit of *m*/*z* < 6000. To explore the presence of heavier particles and possible agglomeration/flocculation processes, we applied dynamic light scattering (DLS) and high resolution transmission electron microscopy (HRTEM). Specifically, we compared HRTEM images of pure $[Ag_{29}]^{3-}$ NCs with those of reaction mixtures after addition of R1S$_2$H$_2$ (at a molar ratio of 0.14)-upon drop casting and air-drying of the respective solutions in acetonitrile onto an amorphous carbon-coated TEM grid. HRTEM images were acquired under gentle TEM imaging conditions, using an accelerating voltage of 100 kV, and frame exposure of <30 s to minimize beam-induced damage or aggregation.[68] Figure 4A shows TEM micrographs for parent NC (i) and R1S$_2$H$_2$-$[Ag_{29}]$ adduct samples (ii-iii), respectively. Whereas Figure 4A(i) shows only discrete NCs as expected for a dried solution of the pure material, Figure 4A (ii) and (iii) manifest aggregated dark spots consisting of multiple $[Ag_{29}]$ cores surrounded by an amorphous carbonaceous, soot-like material.

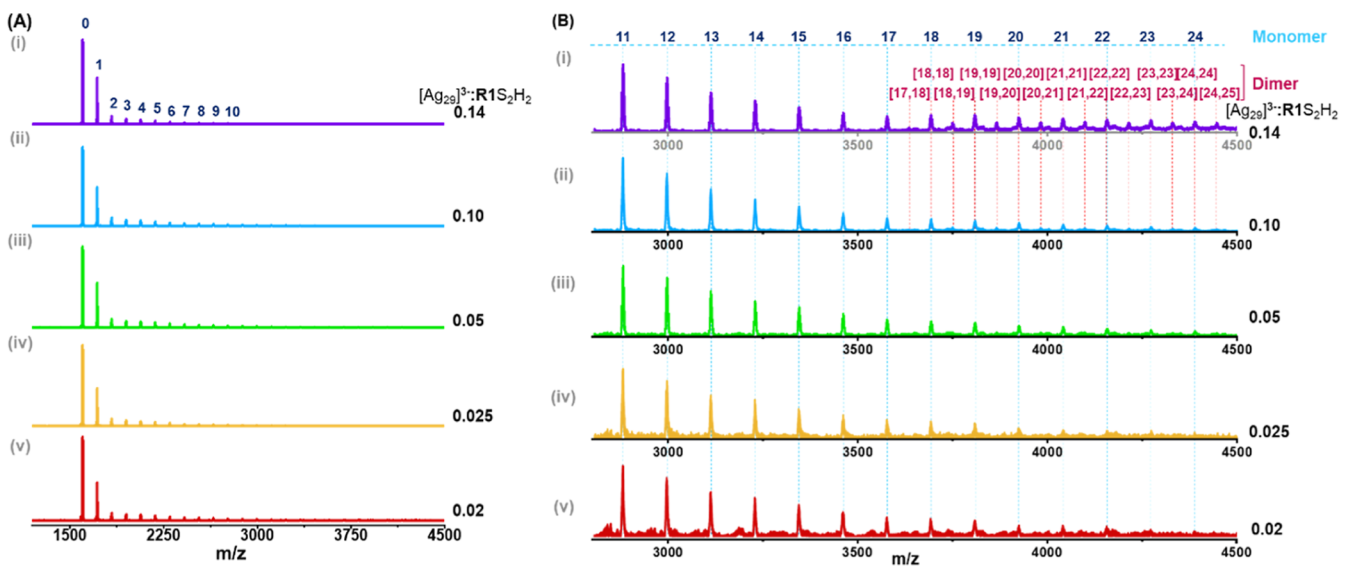

Figure 3. (A) Dependence of full range ESI MS on the ratio of $[Ag_{29}]^{3-}$:R1S$_2$H$_2$ (within 60 s after mixing). Peaks are labeled by the nominal number of attached R1S$_2$H$_2$ ligands. (B) Expanded range segments of these MS for *m*/*z* = 2800−4500. Numbers along the *y*-axes: corresponding reactant molar ratios ranging from 0.14−0.02 (while keeping the concentration of $[Ag_{29}]^{3-}$ constant).

https://doi.org/10.1021/acsnano.6c03086
ACS Nano XXXX, XXX, XXX−XXX

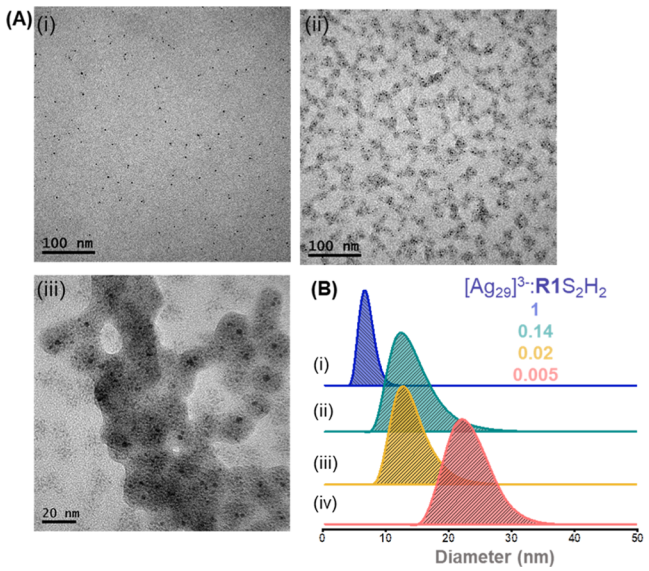

Figure 4. (A) (i) HRTEM micrograph of parent $[Ag_{29}]$ without additional ligand $R1S_2H_2$, (ii) and (iii) HRTEM micrographs at different magnification/scale bars of $R1S_2H_2$-added to $[Ag_{29}]^{3-}$ at a molar ratio of 0.14. (B) DLS measurements showing solution-phase growth of adducts as a function of $R1S_2H_2$ concentration.

Notably, for the $[Ag_{29}]^{3-}$:$\mathbf{R1}S_2H_2$ = 0.14 mixture, we observed no special preponderance of dimer-like aggregates (as seen in ESI-MS). This implies that during solution aging, further NC aggregation occurs outside of the mass spectrometrically observable range. HRTEM micrographs corresponding to solutions prepared with varying $[Ag_{29}]^{3-}$:$\mathbf{R1}S_2H_2$ ratios (i.e., 0.14, 0.02, and 0.01) are shown in Figure S6. The solution phase growth of such bigger NCs with increasing $\mathbf{R1}S_2H_2$ concentration was also explored by dynamic light scattering (DLS) as shown in Figure 4B. DLS measurements indicate spontaneous growth of the average hydrodynamic radii of scatterers (diameter increases from ca. 8 to 23 nm) upon increasing $\mathbf{R1}S_2H_2$ concentration in solution.[14,62,69] Together these measurements confirm the formation of larger-sized particles in solution both upon increasing $\mathbf{R1}S_2H_2$ concentration and upon solution aging.

Docking Simulations and High Level DFT Calculations

To support the experimental findings, we employed molecular docking and quantum chemical calculations to investigate the adsorption behavior and structural evolution of $[Ag_{29}]^{3-}$ with $\mathbf{R1}S_2H_2$ ligands. In addition, we used electrostatic modeling to estimate the coverage dependence of secondary ligand binding energies on NC monomers and to explore the stability of hexaanion dimers in the gas phase. The adsorption process on $[Ag_{29}]^{3-}$ begins with physisorption, where $\mathbf{R1}S_2H_2$ ligands interact with the NC surface via vdW forces. These initial interactions do not involve hydrogen loss and result in the formation of $[Ag_{29}](\mathbf{R1}S_2H_2)_n^{3-}$ adducts. To model this, we used the aISS docking algorithm implemented in xtb[70] to sequentially add neutral $\mathbf{R1}S_2H_2$ ligands to $[Ag_{29}]^{3-}$ up to $[Ag_{29}](\mathbf{R1}S_2H_2)_{16}^{3-}$, i.e.

$$[Ag_{29}]^{3-} + \mathbf{R1}S_2H_2 \rightarrow [Ag_{29}](\mathbf{R1}S_2H_2)_1^{3-}$$

$$[Ag_{29}](\mathbf{R1}S_2H_2)_1^{3-} + \mathbf{R1}S_2H_2 \rightarrow [Ag_{29}](\mathbf{R1}S_2H_2)_2^{3-}$$

...

$$[Ag_{29}](\mathbf{R1}S_2H_2)_{15}^{3-} + \mathbf{R1}S_2H_2 \rightarrow [Ag_{29}](\mathbf{R1}S_2H_2)_{16}^{3-}$$

Geometry optimizations during docking were carried out using the GFN1-xTB method[71] as GFN2-xTB[72] encountered convergence issues. The $\mathbf{R1}S_2H_2$ ligand exists in both *cis* and *trans* configurations (Figure S7), with the *cis* form slightly favored in acetonitrile ($\Delta G \approx 0.017$ eV; see Supporting Information for further details). Importantly, the rotational barrier between the *cis* and *trans* configurations is low (≈0.08 eV), indicating that both forms are accessible. However, the *cis* configuration was found to coordinate more effectively, saturating two Ag coordination sites, and was thus considered further in this study.

Figure 5A–D presents representative docked structures of $[Ag_{29}](\mathbf{R1}S_2H_2)_n^{3-}$ for physisorbed ligand counts n = 4, 8, 12,

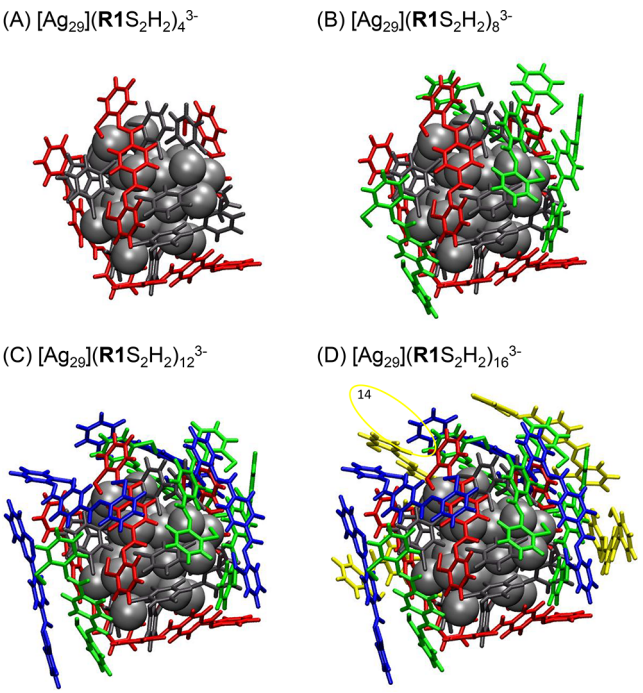

Figure 5. Growth of the $R1S_2H_2$ secondary ligand shell around the $[Ag_{29}]^{3-}$ NC with n = 4 (A); n = 8 (B); n = 12 (C) and n = 16 (D), respectively as derived from GFN1-xTB docking simulations assuming physisorption. Color code: Ag: gray; BDT ligands: black; n = 1–4, red: n = 5–8, green; n = 9–12, blue; n = 13–16, yellow.

and 16, illustrating the progressive assembly and spatial arrangement of the ligands around the NC. The $\mathbf{R1}S_2H_2$ ligands typically orient their central benzene rings *tangentially* to the NC surface, and the *cis* configuration was preserved in all structures. Interestingly, the $\mathbf{R1}S_2H_2$ ligands do not bind to the exposed tetrahedral ^{t}Ag atoms (shielded by PPh_3 ligands in the solid state), but instead coordinate to two crown ^{c}Ag atoms forming Ag–S bonds of ≈2.7 Å length. The ^{t}Ag atoms are positioned beneath the central benzene ring (see Figure S8A) and steric hindrance from BDT ligands prevents simultaneous Ag–S binding to ^{t}Ag sites. While S–Ag coordination dominates, one ligand in $[Ag_{29}](\mathbf{R1}S_2H_2)_4^{3-}$ shows significantly shorter N–Ag distances (2.55 Å and 3.36 Å) compared to its Ag–S distances (4.20 and 5.08 Å), suggesting that N–Ag interactions are also possible (see Figure S8B).

https://doi.org/10.1021/acsnano.6c03086
ACS Nano XXXX, XXX, XXX–XXX

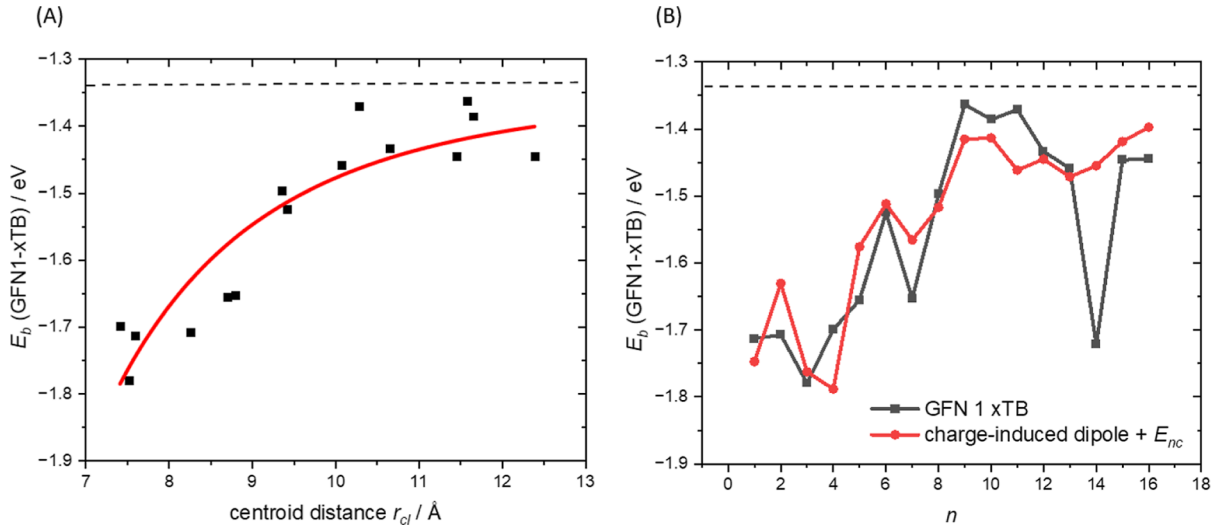

Figure 6. (A) Ligand binding energy from GFN1 xTB docking simulations as a function of the ligand centroid distance. The red line shows a fit according to eq 2. The data point for n = 14 was excluded for the fit due to its unusual binding motif (see text). (B) GFN1 xTB ligand binding energies as a function of the number of adsorbed ligands n. The red curve shows binding energies according to eq 2 calculated with ε_r = 1.9, E_{nc} = −1.34 eV and α = 39.7 × 10^{-30} m^3 (at the centroid distances obtained from the xTB calculations for a specific n). Dotted lines refer to E_{nc} = −1.34 eV.

The centroid distance r_{cl}—from the ligand centroid to the central icosahedral Ag atom—increases from ≈7.5 Å in the first layer to ≈11 Å in the second layer (blue ligands in Figure 5), which begins to form at around n = 9, and reaches ≈12.3 Å at n = 16. Ligands in the second shell are noncovalently bound mainly via vdW interactions (as shown in Figure S9) and form stacked structures reminiscent of *carbon soot particles*.[73,74]

Ligand binding energies up to secondary ligand counts of n = 16 in the gas phase were estimated using GFN1-xTB, without thermostatistical corrections due to computational limitations. The binding energy per ligand was calculated as

$$E_b = E([Ag_{29}](\mathbf{R1}S_2H_2)_n^{3-}) - (E([Ag_{29}](\mathbf{R1}S_2H_2)_{n-1}^{3-}) + E(\mathbf{R1}S_2H_2)) \quad (1)$$

The dependence of the ligand binding energy on the centroid distance r_{cl} is shown in Figure 6A.

Electrostatic Modeling

The GFN1-xTB binding energy decreases with increasing r_{cl}, consistent with a simplified model that combines a distance-dependent ion-induced dipole energy and a distance-independent energy E_{nc}, approximating noncovalent short-range contributions, either between the ligand and the surface of $[Ag_{29}]^{3-}$ or between the ligand and other proximal ligands. Accordingly, the red line in Figure 6A represents a fit to the GFN1-xTB binding energy based on eq 2.

$$E_b = \frac{-1}{4\pi\varepsilon_0\varepsilon_r}\frac{(ze)^2\alpha}{2r_{cl}^4} + E_{nc} \quad (2)$$

in eq 2, ε_0 is the vacuum permittivity (8.854 × 10^{-12} $F.m^{(-1)}$ (= F/m)), ze = −3 × 1.6022 × 10^{-19} C is the charge of the NC (that we assume to be localized in its center), α is the polarizability volume of the ligand (39.7 × 10^{-30} m^3 as calculated with GFN2-xTB), and r_{cl} is the centroid distance. The permittivity ε_r approximates charge shielding effects and was used as a fit parameter together with E_{nc}. In principle, charge−dipole interactions are also possible, but as the dipole moment of the ligand is oriented orthogonally to the electric field, this contribution is expected to be negligible. The best fit was achieved with ε_r = 1.9 and E_{nc} = −1.34 eV. Figure 6B shows the GFN1-xTB binding energies alongside the values from eq 2, plotted as a function of the ligand number, n. The centroid distances used in the calculation were obtained from the GFN1-xTB structures, with ε_r = 1.9 and E_{nc} = −1.34 eV taken from the fitted model. Despite the simplicity of the model, it reproduces the trend of decreasing binding energy with increasing centroid distance r_{cl} quite well. This trend reflects the weakening of the ion-induced dipole interaction as ligands are added further away from the NC center. The fitted value of ε_r = 1.9 is reasonable, as similar values (ε_r = 2−3) have been reported for self-assembled monolayers.[75] The noncovalent binding energy E_{nc} = −1.34 eV is also plausible as the GFN1-xTB binding energy between two neutral ligands forming a $(\mathbf{R1}S_2H_2)_2$ dimer is −1.01 eV while the binding energy between two such $(\mathbf{R1}S_2H_2)_2$ stacks is −0.88 eV (Figure S9). This energy range can be considered a lower limit for the vdW binding energy of ligands in the outer shells, which are stabilized by noncovalent interactions between aromatic moieties, traditionally referred to as π−π stacking, though more accurately described as electrostatic and dispersion−driven interactions.[76] However, dispersion interactions are highly sensitive to ligand orientation within the shell. The higher GFN1-xTB binding energy for ligand n = 14 may be due to its location in a pocket-like structure (see Figure 5D), which enhances vdW interactions.

The GFN1-xTB binding energy of the first $\mathbf{R1}S_2H_2$ ligand to $[Ag_{29}]^{3-}$ is −1.71 eV, with a corresponding binding free energy of −0.95 eV. While this relatively high thermodynamic stability suggests that ligand addition to the $[Ag_{29}]^{3-}$ cluster should drive substantial consumption of $[Ag_{29}]^{3-}$, the largest peak in the mass spectrum (Figure 2) belongs to $[Ag_{29}]^{3-}$. To investigate this contradiction, we reoptimized $[Ag_{29}]^{3-}$ and $[Ag_{29}](\mathbf{R1}S_2H_2)_1^{3-}$ with the r^{2}SCAN-3c composite DFT method and computed free energies by including accurate ωB97X-V/def2-TZVP single-point energies (see Figure S10). The resulting gas phase free binding energy of one $\mathbf{R1}S_2H_2$ ligand in *cis* configuration is −0.64 eV, which qualitatively

https://doi.org/10.1021/acsnano.6c03086
ACS Nano XXXX, XXX, XXX−XXX

matches the GFN1-xTB values but still seemingly contradicts the experiment.

However, considering that the ligand adsorption occurs in solution, solvation contributions may play an important role. To investigate this, we computed the association/adsorption free energy in solution, obtaining a value of 0.32 eV. Although some error is to be expected when applying implicit solvent models for electronically complex and charged species such as $[Ag_{29}]^{3-}$, the result suggests that association is less favorable in solution than in the gas phase, possibly explaining the higher mass spectral peak intensity of $[Ag_{29}]^{3-}$ compared to $[Ag_{29}](\mathbf{R1}S_2H_2)_1^{3-}$.

For the experimental cluster concentration of 50 μM and a cluster-to-ligand ratio of 0.14, the ligand concentration is approximately 357 μM. With ΔG° = 0.32 eV, this gives an estimated $[Ag_{29}](\mathbf{R1}S_2H_2)_1^{3-}$:$[Ag_{29}]^{3-}$ ratio of only $\approx 1.4\times10^{-9}$ in a simple mass–action equilibrium model. Thus, while the positive solution-phase adsorption free energy is qualitatively consistent with the dominance of the parent $[Ag_{29}]^{3-}$ peak and suggests that adsorption of the first isolated ligand is endergonic in solution, the experimentally observed adduct signals cannot be quantitatively explained by this simplified first-step bulk-solution equilibrium alone. Possible contributions include incomplete representation of counterions and explicit solvent molecules, alternative adsorption sites, adduct stabilization during desolvation or gas phase transfer, differences in mass-spectrometric response or survival factors, and possible aggregation or precipitation of higher adducts. Therefore, the observed adduct intensities should be interpreted as apparent abundances rather than direct quantitative solution-phase equilibrium populations. The DFT-optimized structure of $[Ag_{29}](\mathbf{R1}S_2H_2)_1^{3-}$ is shown in Figure S10A, with S–Ag bond lengths of 2.91 Å and 3.11 Å, respectively.

Disulfide Bond Formation

To investigate whether disulfide bond formation-as indirectly evidenced by H_2 loss-could be initiated by proton transfer, involving the $\mathbf{R1}S_2H_2$ ligand and one $[Ag_{29}]^{3-}$ cluster, we tested several proton placement sites. When a proton was positioned near a free Ag site, geometry optimization using the r^{2}SCAN-3c method showed that the proton spontaneously returned to the ligand, indicating an unstable configuration. In contrast, protonation of a BDT moiety by the $\mathbf{R1}S_2H_2$ ligand leads to a stable structure with S–Ag bond lengths of 2.91 Å (Ag-SH) and 2.46 Å (Ag–S). However, this configuration was energetically unfavorable (0.89 eV higher in acetonitrile and 1.53 eV in the gas phase) compared to the physisorption $\mathbf{R1}S_2H_2$ ligand. While these results suggest that direct proton transfer as a first step is unlikely to initiate disulfide bond formation, other species present in solution-such as metal ions or dissolved oxygen-may be responsible for oxidative disulfide formation.[77,78] It also remains unclear whether disulfide bond formation occurs at the ligand-$[Ag_{29}]^{3-}$ interface, within the outer ligand shell, between the ligand shells of two clusters or at all of these positions.

Coulomb Repulsion and Dimer Stability

In the mass spectra, dimeric species of $[Ag_{29}](\mathbf{R1}S_2H_2)_n^{3-}$ are only observed for ligand counts $n \geq 17$. This threshold likely reflects a critical ligand shell thickness that increases the center-to-center distance between $[Ag_{29}](\mathbf{R1}S_2H_2)_n^{3-}$ monomers, thereby reducing the Coulombic repulsion to a level where dimer stabilization becomes feasible. At lower ligand coverage, the electrostatic repulsion dominates, likely causing dimers made up of smaller (trianionic) monomers to dissociate in the gas phase, even if formed in solution. Similar aspects were recently discussed in a photoelectron spectroscopy study of $[MAu_{24}(SC_nH_{2n+1})_{18}]^-$ (M = Au, Pt; n = 6, 8, 10, 12) cluster dimers.[31]

To estimate the electrostatic Coulomb repulsion between two $[Ag_{29}](\mathbf{R1}S_2H_2)_n^{3-}$ monomers, we again apply a simplified electrostatic model and calculate the repulsion energy as

$$E_c = \frac{1}{4\pi\varepsilon_0\varepsilon_r}\frac{(-3e)^2}{r_{cc}} \quad (3)$$

here, ε_r = 1.9 is taken from the earlier fit and r_{cc} is the center-to-center distance between two monomers, i.e. $r_{cc} = 2\ r_{cl} + r_s$, where r_{cl} is the centroid distance of the outermost ligand as defined above and $r_s \approx 3.6$ Å is the typical separation between the ligand layers. The Coulomb repulsion energy E_{cr} is shown in Figure 7 as a function of r_{cc} with values at n = 4, 8,12, and 16

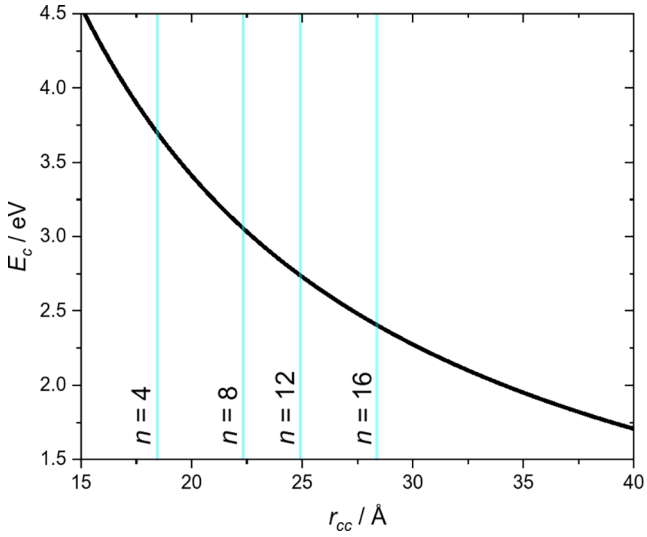

Figure 7. Centre-to-center distance vs calculated repulsive Coulomb energy in a hypothetical NC dimer hexaanion according to eq 3. The highlighted numerical values denote the number of $\mathbf{R1}S_2H_2$ present in the $[Ag_{29}](\mathbf{R1}S_2H_2)_n^{3-}$ NC monomers at the corresponding separation.

highlighted. At n = 16-the range where dimers tend to be stable in the gas phase-the repulsion energy reaches ≈2.4 eV. For dimer formation to occur at this stage, this repulsive energy must be compensated by the attractive interaction between ligands in the outer shells of each NC. Most likely this arises from vdW and/or disulfide bonds between two ligands, each bound to a different $[Ag_{29}](\mathbf{R1}S_2H_2)_n^{3-}$ monomer. The balance between these attractive and repulsive forces determines the feasibility of dimer formation at high ligand coverage.[79]

To further assess the feasibility of dimer formation, we discuss the relative energetic contributions of vdW interactions and disulfide bond formation between ligands in the outer shells of two interacting adsorbate covered NCs. To first approximation, the vdW binding energy between two adjacent $\mathbf{R1}S_2H_2$ ligands in the respective outer shells can be modeled as the energy required to cleave a stacked $(\mathbf{R1}S_2H_2)_n$ aggregate (Figure S9). At the GFN1-xTB level this energy ranges somewhere between −0.88 eV (for cleavage of $(\mathbf{R1}S_2H_2)_4$ into

https://doi.org/10.1021/acsnano.6c03086
ACS Nano XXXX, XXX, XXX–XXX

two $(\mathbf{R1}S_2H_2)_2$ dimers) and −1.01 eV (for cleavage of $(\mathbf{R1}S_2H_2)_2$)—i.e. much less than the Coulomb repulsion energy. Consequently, more secondary ligand interactions including also cooperative effects, (e.g., interlocking to maximize contact area) would have to be postulated. Alternatively, additional stabilization through (intercluster) disulfide bond formation-as indirectly supported by the observation of H atom loss-might become a critical factor in increasing the binding energy beyond the Coulombic repulsion between adjacent monomers. Typical disulfide bond energies of multisubstituted diphenyldisulfides are ≈50 kcal/mol (≈2.2 eV) which together with one $\mathbf{R1}S_2H_2{\cdot}\mathbf{R1}S_2H_2$ vdW interaction would raise the total attractive interaction energy to approximately 3 eV, making NC dimer formation energetically favorable even in the presence of significant electrostatic repulsion.[80,81]

CONCLUSIONS

We have used experiment and theory to explore the supramolecular adsorption of secondary dithiol ligands, $\mathbf{R1}S_2H_2$, onto monolayer protected atomically precise $[Ag_{29}]^{3-}$ NC in acetonitrile solution under ambient conditions. High resolution anion electrospray mass spectrometry shows rapid adduct formation upon introduction of the dithiol into the NC solution (within 60 s after mixing). Systematic variation of reagent molar ratios indicates that under optimum conditions (for a $[Ag_{29}]^{3-}$:$\mathbf{R1}S_2H_2$ molar ratio of 0.14) individual NC can bind up to ≈28 secondary ligands. These conditions also lead to rapid intercluster dimerization. Corresponding dimers are observed (by mass spectrometry) between NC monomers having more than 16 secondary ligand adsorbates. Increasing the relative $\mathbf{R1}S_2H_2$ concentration further induces degradation/fragmentation of the monomeric NCs.

High resolution mass spectrometry confirms that the secondary dithiols attached to $[Ag_{29}]^{3-}$ are mostly physisorbed. Over the course of up to 270 min, however, they progressively convert into chemisorptive species, accompanied by the loss of multiple H atoms. We speculate that this involves $\mathbf{R1}S_2H_2$ deprotonation in solution via redox reactions of adsorbate covered NC multianions with adventitious oxidants (such as dissolved O_2).

Computational modeling was performed to understand the details of secondary ligand adsorption. This indicates that adsorption is associated with stepwise growth of a soot-particle-like dithiol shell around the individual NCs. In turn, this makes plausible the formation of dimeric structures above a specific adsorbate coverage beyond which Coulomb repulsion is compensated by interligand cohesion. Moreover, DLS studies and HRTEM imaging imply that continued solution interaction of $\mathbf{R1}S_2H_2$ adsorbates on different $[Ag_{29}]^{3-}$ clusters leads to further aggregation of soot-like particles beyond the dimer stage (at the mass detection limit of electrospray MS).

Our observation of a mechanistic separation between fast supramolecular adsorption/dimerization and slower chemisorptive cross-linking processes as induced by tangentially binding "rigid" $\mathbf{R1}S_2H_2$ secondary ligands of length comparable to the $[Ag_{29}]^{3-}$ diameter suggests a new general framework for controlling the assembly of cluster materials. Correspondingly, exploiting tunable secondary ligand design concepts, redox control, and external stimuli will allow improved access to cluster-to-material transformations of interest for nanoarchitectonics applications.

METHODS

Instrumentation

High-resolution ESI MS measurements were performed using two different high-resolution mass spectrometers, namely—a Synapt G2 Si (Waters, Manchester, U.K.) at IIT Madras, and a timsTOF (Bruker Daltonics, Bremen, Germany) at KIT. These two mass spectrometers were utilized as they complement each other. The high resolution timsTOF instrument was utilized to study the time dependence of ligand adsorptions in solution and to detect slight changes in m/z during H-loss. Conversely, the Synapt G2-Si mass spectrometer was employed under soft-ionization conditions to detect weakly bound dimers.

The following parameters were applied for the Synapt G2-Si mass spectrometer—capillary voltage: 2—2.5 kV, sample cone: 10 V, source offset: 10 V, trap gas flow: 3 mL/min, desolvation gas flow: 500 L/h, desolvation gas temperature: 150° C, source temperature: 100° C and the sample concentration was 1 μg/mL in acetonitrile solvent and infused at a flow rate of 20 μL/min. In timsTOF, the electrosprayed ions were generated by applying the following parameters—capillary voltage: 5 kV, nebulizer gas flow: 0.3 bar, dry gas flow: 3 L/min, dry gas temperature: 200° C. ESI flow rate was set at 100 μL/h. All parameters were systematically optimized to minimize ion loss and in-source fragmentation.

Theoretical Calculation

For the calculations involving $[Ag_{29}]^{3-}$ we used the X-ray structure of $[Ag_{29}(BDT)_{12}(PPh_3)_4]$ (without the PPh_3 units) as a starting point.[1] The docking simulation studies—in which we docked up to 16 neutral $\mathbf{R1}S_2H_2$ ligands in a sequential manner to $[Ag_{29}]^{3-}$-were performed with the aISS docking algorithm as implemented in xtb (version 6.6.0)[2] combined with GFN1-xTB[3] for final geometry optimizations. To generate different conformers of the $\mathbf{R1}S_2H_2$ ligand, we used the Conformer-Rotamer Ensemble Sampling Tool CREST version 2.12,[4] employing GFN2-xTB[5] and for the solvated structures the ALPB[6] implicit solvation model was used additionally. Subsequent DFT refinement was done with CENSO 1.2.0[7] employing the r^{2}SCAN-3c[8] method. For modeling solvation during the refinement, the implicit solvent model CPCM was used during the geometry optimizations and COSMO-RS[9] with the BP TZVP C30 1601 parametrization for computing the solvation free energies. The input for the COSMOtherm program package was thereby generated from two TURBOMOLE[10] 7.5.1 single-point calculations with BP86[11,12]/def-TZVP[13] (one in the gas phase and one in an ideal conductor). The ideal conductor is modeled by applying the COSMO model with a dielectric constant set to infinity.

The information from gas phase and ideal conductor calculations is then combined to compute the COSMO-RS solvation free energy. Also, structures of $[Ag_{29}](\mathbf{R1}S_2H_2)_n^{3-}$ with n = 0—1 were refined by DFT optimizations using r^{2}SCAN-3c.[8] Free energies of these structures and the ligand conformers were calculated with ωB97X-V[14]/def2-TZVP[15] electronic energies, and thermal contributions were computed with r^{2}SCAN-3c.[8] The DFT calculations were carried out with ORCA 5.0.4[16] with default settings.

ASSOCIATED CONTENT

Supporting Information

The Supporting Information is available free of charge at https://pubs.acs.org/doi/10.1021/acsnano.6c03086.

Reagents and materials, synthesis of NC and $\mathbf{R1}S_2H_2$, and additional figures including negative mode full range ESI MS, HRTEM micrographs, GFN2 xTB optimized structures, and the DFT optimized structures (PDF)

https://doi.org/10.1021/acsnano.6c03086
ACS Nano XXXX, XXX, XXX−XXX

AUTHOR INFORMATION

Corresponding Authors

Thalappil Pradeep − *DST Unit of Nanoscience & Thematic Unit of Excellence, Department of Chemistry, Indian Institute of Technology Madras, Chennai 600036, India; International Centre for Clean Water, Taramani, Chennai 600113, India;* orcid.org/0000-0003-3174-534X; Email: pradeep@iitm.ac.in; Fax: 91-44-2257-0545/0509

Manfred M. Kappes − *Institute of Physical Chemistry, Karlsruhe Institute of Technology, Karlsruhe 76131, Germany; Institute of Nanotechnology, Karlsruhe Institute of Technology, Karlsruhe 76131, Germany;* orcid.org/0000-0002-1199-1730; Email: manfred.kappes@kit.edu

Authors

Jayoti Roy − *DST Unit of Nanoscience & Thematic Unit of Excellence, Department of Chemistry, Indian Institute of Technology Madras, Chennai 600036, India; Institute of Physical Chemistry, Karlsruhe Institute of Technology, Karlsruhe 76131, Germany;* orcid.org/0009-0006-6535-0011

Marco Neumaier − *Institute of Physical Chemistry, Karlsruhe Institute of Technology, Karlsruhe 76131, Germany; Institute of Nanotechnology, Karlsruhe Institute of Technology, Karlsruhe 76131, Germany;* orcid.org/0000-0002-3810-3377

Christoph Plett − *Mulliken Center for Theoretical Chemistry, Clausius-Institut Für Physikalische und Theoretische Chemie, Universität Bonn, Bonn 53115, Germany;* orcid.org/0000-0002-3911-2478

Papri Chakraborty − *Institute of Physical Chemistry, Karlsruhe Institute of Technology, Karlsruhe 76131, Germany; Institute of Nanotechnology and Institute for Quantum Materials and Technologies, Karlsruhe Institute of Technology, Karlsruhe 76131, Germany;* orcid.org/0000-0002-1353-7734

Anirban Som − *DST Unit of Nanoscience & Thematic Unit of Excellence, Department of Chemistry, Indian Institute of Technology Madras, Chennai 600036, India;* orcid.org/0000-0002-6646-679X

Arijit Jana − *DST Unit of Nanoscience & Thematic Unit of Excellence, Department of Chemistry, Indian Institute of Technology Madras, Chennai 600036, India;* orcid.org/0000-0002-5676-0688

Stefan Grimme − *Mulliken Center for Theoretical Chemistry, Clausius-Institut Für Physikalische und Theoretische Chemie, Universität Bonn, Bonn 53115, Germany;* orcid.org/0000-0002-5844-4371

Horst Hahn − *Department of Materials Science and Engineering, The University of Arizona, Tucson, Arizona 85719, United States*

Complete contact information is available at: https://pubs.acs.org/10.1021/acsnano.6c03086

Notes

The authors declare no competing financial interest.

ACKNOWLEDGMENTS

The authors thank the Department of Science and Technology (DST), Government of India for constantly supporting our research program. J.R. and A.J. thank IIT Madras for an institute doctoral fellowship. J.R. also acknowledges partial support by the Gunther-Schroff Foundation and KIT International Excellence Grants. T.P. acknowledges funding from the Centre of Excellence on Molecular Materials and Functions under the Institution of Eminence scheme of IIT Madras. T.P. also acknowledges the Science and Engineering Research Board (SERB) for a J.C. Bose Fellowship (CHY1516331DSTXTPRA) and a Scientific and Useful Profound Research Advancement research grant (SP22230413CYSERB002505). He also thanks the DST for a research grant from the Indo-German Collaborative Activities in Chemistry and Physics scheme (SP20210994CYDSTX002505). M.K. and H.H. acknowledge the German Science Foundation (DFG) for support of a DFG-DST collaborative project under KA 972/11-1 and HA 1344/47-1. C.P. thanks the Merck KGaA for financial support.

REFERENCES

(1) Chakraborty, I.; Pradeep, T. Atomically Precise Clusters of Noble Metals: Emerging Link between Atoms and Nanoparticles. *Chem. Rev.* **2017**, *117* (12), 8208−8271.

(2) Jin, R. Atomically Precise Metal Nanoclusters: Stable Sizes and Optical Properties. *Nanoscale* **2015**, *7* (5), 1549−1565.

(3) Yang, H.; Wang, Y.; Lei, J.; Shi, L.; Wu, X.; Mäkinen, V.; Lin, S.; Tang, Z.; He, J.; Häkkinen, H.; Zheng, L.; Zheng, N. Ligand-Stabilized $Au_{13}Cu_x$ (x = 2, 4, 8) Bimetallic Nanoclusters: Ligand Engineering to Control the Exposure of Metal Sites. *J. Am. Chem. Soc.* **2013**, *135* (26), 9568−9571.

(4) Park, J.-E.; Seo, M.; Jang, E.; Kim, H.; Kim, S.; Park, S.-J. Vesicle-like Assemblies of Ligand-Stabilized Nanoparticles with Controllable Membrane Composition and Properties. *Nanoscale* **2019**, *11*, 1837−1846.

(5) Kurashige, W.; Yamaguchi, M.; Nobusada, K.; Negishi, Y. Ligand-Induced Stability of Gold Nanoclusters: Thiolate versus Selenolate. *J. Phys. Chem. Lett.* **2012**, *3* (18), 2649−2652.

(6) Shibu, E. S.; Muhammed, M. A. H.; Tsukuda, T.; Pradeep, T. Ligand Exchange of $Au_{25}SG_{18}$ Leading to Functionalized Gold Clusters: Spectroscopy, Kinetics, and Luminescence. *J. Phys. Chem. C* **2008**, *112* (32), 12168−12176.

(7) Abubaker, M.; Muhammed, H.; Ramesh, S.; Sinha, S. S.; Kumar Pal, S.; Pradeep, T. Two Distinct Fluorescent Quantum Clusters of Gold Starting from Metallic Nanoparticles by PH-Dependent Ligand Etching. *Nano Research* **2010**, *1* (4), 333−340.

(8) Muhammed, M. A. H.; Shaw, A. K.; Pal, S. K.; Pradeep, T. Quantum Clusters of Gold Exhibiting FRET. *J. Phys. Chem. C* **2008**, *112* (37), 14324−14330.

(9) Matus, M. F.; Häkkinen, H. Understanding Ligand-Protected Noble Metal Nanoclusters at Work. *Nat. Rev. Mater.* **2023**, *8* (6), 372−389.

(10) Taylor, M. G.; Mpourmpakis, G. Rethinking Heterometal Doping in Ligand-Protected Metal Nanoclusters. *J. Phys. Chem. Lett.* **2018**, *9*, 6773−6778.

(11) Tiwari, V.; Karmakar, T. Understanding Molecular Aggregation of Ligand-Protected Atomically-Precise Metal Nanoclusters. *J. Phys. Chem. Lett.* **2023**, *14* (29), 6686−6694.

(12) Niihori, Y.; Matsuzaki, M.; Pradeep, T.; Negishi, Y. Separation of Precise Compositions of Noble Metal Clusters Protected with Mixed Ligands. *J. Am. Chem. Soc.* **2013**, *135* (13), 4946−4949.

(13) Wang, Y.; Bürgi, T. Ligand Exchange Reactions on Thiolate-Protected Gold Nanoclusters. *Nanoscale Adv.* **2021**, *3* (10), 2710−2727.

(14) Roy, J.; Mondal, B.; Vishwakarma, G.; Nonappa; Vasanthi Sridharan, N.; Krishnamurthi, P.; Pradeep, T. Dissociative Reactions of $[Au_{25}(SR)_{18}]^-$ at Copper Oxide Nanoparticles and Formation of Aggregated Nanostructures. *Nanoscale* **2023**, *15* (18), 8225−8234.

(15) Dass, A.; Stevenson, A.; Dubay, G. R.; Tracy, J. B.; Murray, R. W. Nanoparticle MALDI-TOF Mass Spectrometry without Fragmentation: $Au_{25}(SCH_2CH_2Ph)_{18}$ and Mixed Monolayer

https://doi.org/10.1021/acsnano.6c03086
ACS Nano XXXX, XXX, XXX−XXX

$Au_{25}(SCH_2CH_2Ph)_{18-x}(L)_X$. *J. Am. Chem. Soc.* **2008**, *130* (18), 5940−5946.
(16) Surman, A. J.; Robbins, P. J.; Ujma, J.; Zheng, Q.; Barran, P. E.; Cronin, L. Sizing and Discovery of Nanosized Polyoxometalate Clusters by Mass Spectrometry. *J. Am. Chem. Soc.* **2016**, *138* (11), 3824−3830.
(17) Doussineau, T.; Yu Bao, C.; Clavier, C.; Dagany, X.; Kerleroux, M.; Antoine, R.; Dugourd, P. Infrared Multiphoton Dissociation Tandem Charge Detection-Mass Spectrometry of Single Megadalton Electrosprayed Ions. *Rev. Sci. Instrum.* **2011**, *82* (8), 084104.
(18) Pradeep, T. *Atomically Precise Metal Nanoclusters*, 1 ed.; Elsevier, 2023..
(19) Krishnadas, K. R.; Baksi, A.; Ghosh, A.; Natarajan, G.; Pradeep, T. Structure-Conserving Spontaneous Transformations between Nanoparticles. *Nat. Commun* **2016**, *7* (1), 1−9.
(20) Krishnadas, K. R.; Ghosh, A.; Baksi, A.; Chakraborty, I.; Natarajan, G.; Pradeep, T. Intercluster Reactions between $Au_{25}(SR)_{18}$ and $Ag_{44}(SR)_{30}$. *J. Am. Chem. Soc.* **2016**, *138* (1), 140−148.
(21) Sooraj, B. S.; Roy, J.; Mukherjee, M.; Jose, A.; Pradeep, T. Extensive Polymerization of Atomically Precise Alloy Metal Clusters During Solid-State Reactions. *Langmuir* **2024**, *40* (29), 15244−15251.
(22) Neumaier, M.; Baksi, A.; Weis, P.; Schneider, E. K.; Chakraborty, P.; Hahn, H.; Pradeep, T.; Kappes, M. M. Kinetics of Intercluster Reactions between Atomically Precise Noble Metal Clusters $[Ag_{25}(DMBT)_{18}]^-$ and $[Au_{25}(PET)_{18}]^-$ in Room Temperature Solutions. *J. Am. Chem. Soc.* **2021**, *143* (18), 6969−6980.
(23) Yang, L.; Cheng, H.; Jiang, Y.; Huang, T.; Bao, J.; Sun, Z.; Jiang, Z.; Ma, J.; Sun, F.; Liu, Q.; Yao, T.; Deng, H.; Wang, S.; Zhu, M.; Wei, S. In Situ Studies on Controlling an Atomically-Accurate Formation Process of Gold Nanoclusters. *Nanoscale* **2015**, *7* (34), 14452−14459.
(24) Baksi, A.; Schneider, E. K.; Weis, P.; Chakraborty, I.; Fuhr, O.; Lebedkin, S.; Parak, W. J.; Kappes, M. M. Linear Size Contraction of Ligand Protected Ag_{29} Clusters by Substituting Ag with Cu. *ACS Nano* **2020**, *14* (11), 15064−15070.
(25) Tang, L.; Kang, X.; Wang, X.; Zhang, X.; Yuan, X.; Wang, S. Dynamic Metal Exchange between a Metalloid Silver Cluster and Silver(I) Thiolate. *Inorg. Chem.* **2021**, *60* (5), 3037−3045.
(26) Chakraborty, P.; Nag, A.; Natarajan, G.; Bandyopadhyay, N.; Paramasivam, G.; Panwar, M. K.; Chakrabarti, J.; Pradeep, T.; Kumar Panwar, M.; Chakrabarti, J.; Pradeep, T. Rapid Isotopic Exchange in Nanoparticles. *Sci. Adv.* **2019**, *5* (1), No. eaau7555.
(27) Chakraborty, P.; Baksi, A.; Mudedla, S. K.; Nag, A.; Paramasivam, G.; Subramanian, V.; Pradeep, T. Understanding Proton Capture and Cation-Induced Dimerization of $[Ag_{29}(BDT)_{12}]^{3-}$ Clusters by Ion Mobility Mass Spectrometry. *Phys. Chem. Chem. Phys.* **2018**, *20* (11), 7593−7603.
(28) Nag, A.; Chakraborty, P.; Bodiuzzaman, M.; Ahuja, T.; Antharjanam, S.; Pradeep, T. Polymorphism of $Ag_{29}(BDT)_{12}(TPP)_4^{3-}$ Cluster: Interactions of Secondary Ligands and Their Effect on Solid State Luminescence. *Nanoscale* **2018**, *10* (21), 9851−9855.
(29) Liang, X. Q.; Li, Y. Z.; Wang, Z.; Zhang, S. S.; Liu, Y. C.; Cao, Z. Z.; Feng, L.; Gao, Z. Y.; Xue, Q. W.; Tung, C. H.; Sun, D. Revealing the Chirality Origin and Homochirality Crystallization of Ag_{14} Nanocluster at the Molecular Level. *Nat. Commun* **2021**, *12* (1), 1−10.
(30) Nag, A.; Pradeep, T. Assembling Atomically Precise Noble Metal Nanoclusters Using Supramolecular Interactions. *ACS Nanosci. Au* **2022**, *2* (3), 160−178.
(31) Nakashima, Y.; Ito, S.; Koyasu, K.; Tsukuda, T. Formation of Dimers of $[MAu_{24}(SC_nH_{2\ n+1})_{18}]^-$ (M = Au, Pt; n = 6, 8, 10, 12) in Gas Phase by Overcoming Electrostatic Repulsion through Aurophilic and Multiple VdW Attractions. *J. Phys. Chem. Lett.* **2025**, *16* (27), 6954−6959.
(32) Kang, X.; Zhu, M. Intra-Cluster Growth Meets Inter-Cluster Assembly: The Molecular and Supramolecular Chemistry of Atomically Precise Nanoclusters. *Coord. Chem. Rev.* **2019**, *394*, 1−38.
(33) Nag, A.; Chakraborty, P.; Paramasivam, G.; Bodiuzzaman, M.; Natarajan, G.; Pradeep, T. Isomerism in Supramolecular Adducts of Atomically Precise Nanoparticles. *J. Am. Chem. Soc.* **2018**, *140* (42), 13590−13593.
(34) Shen, H.; Kang, X.; Zhu, M. Derivative Chemistry of Ag_{29} Nanoclusters. *Acc. Mater. Res.* **2025**, *6*, 779−793.
(35) Wei, X.; Huang, Z.; Sun, X.; Li, H.; Sun, Z.; Tang, Q.; Zhu, L.; Kang, X.; Zhu, M. Atomically Defined Two-Dimensional Assembled Nanoclusters for Li-Ion Batteries. *Nat. Synth.* **2025**, *4* (11), 1349−1358.
(36) Chakraborty, P.; Nag, A.; Chakraborty, A.; Pradeep, T. Approaching Materials with Atomic Precision Using Supramolecular Cluster Assemblies. *Acc. Chem. Res.* **2019**, *52* (1), 2−11.
(37) Sahoo, K.; Gazi, T. R.; Roy, S.; Chakraborty, I. Nanohybrids of Atomically Precise Metal Nanoclusters. *Commun. Chem* **2023**, *6* (1), 1−14.
(38) O'Brien, E. S.; Trinh, M. T.; Kann, R. L.; Chen, J.; Elbaz, G. A.; Masurkar, A.; Atallah, T. L.; Paley, M. V.; Patel, N.; Paley, D. W.; Kymissis, I.; Crowther, A. C.; Millis, A. J.; Reichman, D. R.; Zhu, X. Y.; Roy, X. Single-Crystal-to-Single-Crystal Intercalation of a Low-Bandgap Superatomic Crystal. *Nat. Chem.* **2017**, *9* (12), 1170−1174.
(39) Huang, J. H.; Liu, L. Y.; Wang, Z. Y.; Zang, S. Q.; Mak, T. C. W. Modular Cocrystallization of Customized Carboranylthiolate-Protected Copper Nanoclusters via Host-Guest Interactions. *ACS Nano* **2022**, *16* (11), 18789−18794.
(40) Roy, J.; Das, A.; Jana, A.; Chakraborty, P.; Neumaier, M.; Hahn, H.; Pathak, B.; Kappes, M. M.; Pradeep, T. Structural Changes in Atomically Precise Ag_{29} Nanoclusters upon Sequential Attachment and Detachment of Secondary Ligands. *ACS Nano* **2025**, *19* (5), 5727−5738.
(41) Li, H.; Wang, P.; Zhu, C.; Zhang, W.; Zhou, M.; Zhang, S.; Zhang, C.; Yun, Y.; Kang, X.; Pei, Y.; Zhu, M. Triple-Helical Self-Assembly of Atomically Precise Nanoclusters. *J. Am. Chem. Soc.* **2022**, *144* (50), 23205−23213.
(42) Yang, H.; Wang, Y.; Huang, H.; Gell, L.; Lehtovaara, L.; Malola, S.; Häkkinen, H.; Zheng, N. All-Thiol-Stabilized Ag_{44} and $Au_{12}Ag_{32}$ Nanoparticles with Single-Crystal Structures. *Nat. Commun.* **2013**, *4* (1), 1−8.
(43) AbdulHalim, G.; Bootharaju, M. S.; Tang, Q.; Del Gobbo, S.; AbdulHalim, R. G.; Eddaoudi, M.; Jiang, D.; Bakr, M. O. $Ag_{29}(BDT)_{12}(TPP)_4$: A Tetravalent Nanocluster. *J. Am. Chem. Soc.* **2015**, *137* (37), 11970−11975.
(44) Joshi, C. P.; Bootharaju, M. S.; Alhilaly, J.; Bakr, O. M. O. $[Ag_{25}(SR)_{18}]^-$: The "Golden" Silver Nanoparticle. *J. Am. Chem. Soc.* **2015**, *137* (36), 11578−11581.
(45) Levi-Kalisman, Y.; Jadzinsky, P. D.; Kalisman, N.; Tsunoyama, H.; Tsukuda, T.; Bushnell, D. A.; Kornberg, D. R. Synthesis and Characterization of Au_{102}(p-MBA)$_{44}$ Nanoparticles. *J. Am. Chem. Soc.* **2011**, *133* (9), 2976−2982.
(46) Ghosh, A.; Ghosh, D.; Khatun, E.; Chakraborty, P.; Pradeep, T. Unusual Reactivity of Dithiol Protected Clusters in Comparison to Monothiol Protected Clusters: Studies Using $Ag_{51}(BDT)_{19}(TPP)_3$ and $Ag_{29}(BDT)_{12}(TPP)_4$. *Nanoscale* **2017**, *9* (3), 1068−1077.
(47) Chakraborty, A.; Fernandez, A. C.; Som, A.; Mondal, B.; Natarajan, G.; Paramasivam, G.; Lahtinen, T.; Häkkinen, H.; Häkkinen, H.; Pradeep, T.; Lahtinen, T.; Häkkinen, H.; Fernandez, A. C. Atomically Precise Nanocluster Assemblies Encapsulating Plasmonic Gold Nanorods. *Angew. Chem. Int. Ed.* **2018**, *130*, 6632−6636.
(48) Nonappa; Lahtinen, T.; Haataja, J. S.; Tero, T. R.; Häkkinen, H.; Ikkala, O. Template-Free Supracolloidal Self-Assembly of Atomically Precise Gold Nanoclusters: From 2D Colloidal Crystals to Spherical Capsids. *Angew. Chem. Int. Ed.* **2016**, *55* (52), 16035−16038.
(49) Lahtinen, T.; Hulkko, E.; Sokołowska, K.; Tero, T.-R.; Saarnio, V.; Lindgren, J.; Pettersson, M.; Häkkinen, H.; Lehtovaara, L. Covalently Linked Multimers of Gold Nanoclusters Au_{102}(p-MBA)$_{44}$ and $Au_{\sim 250}$(p-MBA)$_n$. *Nanoscale* **2016**, *8*, 18665.

https://doi.org/10.1021/acsnano.6c03086
ACS Nano XXXX, XXX, XXX−XXX

(50) Kolay, S.; Bain, D.; Maity, S.; Devi, A.; Patra, A.; Antoine, R. Self-Assembled Metal Nanoclusters: Driving Forces and Structural Correlation with Optical Properties. *Nanomaterials* **2022**, *12* (3), 544.
(51) Salassa, G.; Krishnadas, K. R.; Pupier, M.; Viger-Gravel, J.; Bürgi, T. Role of Intercluster and Interligand Dynamics of $[Ag_{25}(DMBT)_{18}]^-$ Nanoclusters by Multinuclear Magnetic Resonance Spectroscopy. *J. Phys. Chem. C* **2021**, *125* (4), 2524−2530.
(52) Krishnadas, K. R.; Baksi, A.; Ghosh, A.; Natarajan, G.; Pradeep, T. Manifestation of Geometric and Electronic Shell Structures of Metal Clusters in Intercluster Reactions. *ACS Nano* **2017**, *11*, 6015−6023.
(53) Baksi, A.; Schneider, E. K.; Weis, P.; Krishnadas, K. R.; Ghosh, D.; Hahn, H.; Pradeep, T.; Kappes, M. M. Nanogymnastics: Visualization of Intercluster Reactions by High-Resolution Trapped Ion Mobility Mass Spectrometry. *J. Phys. Chem. C* **2019**, *123* (46), 28477−28485.
(54) Krishnadas, K. R.; Baksi, A.; Ghosh, A.; Natarajan, G.; Pradeep, T. Structure-Conserving Spontaneous Transformations between Nanoparticles. *Nat. Commun.* **2016**, *7* (13447), 1−9.
(55) Molina, L. M.; Hammer, B. Theoretical Study of Thiol-Induced Reconstructions on the Au(1 1 1) Surface. *Chem. Phys. Lett.* **2002**, *360*, 264−271.
(56) Tielens, F.; Andrés, J.; Van Brussel, M.; Buess-Hermann, C.; Geerlings, P. DFT Study of Oxygen Adsorption on Modified Nanostructured Gold Pyramids. *J. Phys. Chem. B* **2005**, *109*, 7624−7630.
(57) Morikawa, Y.; Liew, C.; Nozoye, H. Methylthiolate Induced Vacancy Formation on Au(1 1 1): A Density Functional Theoretical Study. *Surf. Sci.* **2002**, *514* (1−3), 389−393.
(58) Guesmi, H.; Luque, N. B.; Santos, E.; Tielens, F. Does the S−H Bond Always Break after Adsorption of an Alkylthiol on Au(111)? *Chem—Eur. J.* **2017**, *23* (6), 1402−1408.
(59) Häkkinen, H. The Gold-Sulfur Interface at the Nanoscale. In *Nature Chemistry*; Nature Publishing Group, 2012; pp 443−455. June 22..
(60) Bedford, E.; Humblot, V.; Méthivier, C.; Pradier, C. M.; Gu, F.; Tielens, F.; Boujday, S. An Experimental and Theoretical Approach to Investigate the Effect of Chain Length on Aminothiol Adsorption and Assembly on Gold. *Chem—Eur. J.* **2015**, *21* (41), 14555−14561.
(61) Mazzarello, R.; Cossaro, A.; Verdini, A.; Rousseau, R.; Casalis, L.; Danisman, M. F.; Floreano, L.; Scandolo, S.; Morgante, A.; Scoles, G. Structure of a CH3S Monolayer on Au(111) Solved by the Interplay between Molecular Dynamics Calculations and Diffraction Measurements. *Phys. Rev. Lett.* **2007**, *98* (1), 016102.
(62) Bose, P.; Srikrishnarka, P.; Paatelainen, M.; Nonappa, N.; Kini, A. R.; Som, A.; Pradeep, T. Nanocluster Reaction-Driven in Situ Transformation of Colloidal Nanoparticles to Mesostructures. *Nanoscale* **2025**, *17* (2), 803−812.
(63) Kawawaki, T.; Kataoka, Y.; Hirata, M.; Iwamatsu, Y.; Hossain, S.; Negishi, Y. Toward the Creation of High-Performance Heterogeneous Catalysts by Controlled Ligand Desorption from Atomically Precise Metal Nanoclusters. *Nanoscale Horiz.* **2021**, *6* (6), 409−448.
(64) Du, W.; Deng, S.; Chen, S.; Jin, S.; Zhen, Y.; Pei, Y.; Zhu, M. Anisotropic Evolution of Nanoclusters from Ag40 to Ag45: Halogen- and Defect-Induced Epitaxial Growth in Nanoclusters. *J. Phys. Chem. Lett.* **2021**, *12* (28), 6654−6660.
(65) Adnan, R. H.; Madridejos, J. M. L.; Alotabi, A. S.; Metha, G. F.; Andersson, G. G. A Review of State of the Art in Phosphine Ligated Gold Clusters and Application in Catalysis. *Adv. Sci.* **2022**, *9* (15), 1−48.
(66) Xu, C.; Yuan, Q.; Wei, X.; Li, H.; Shen, H.; Kang, X.; Zhu, M. Surface Environment Complication Makes Ag_{29} Nanoclusters More Robust and Leads to Their Unique Packing in the Supracrystal Lattice. *Chem. Sci.* **2022**, *13*, 1382−1389.
(67) Baksi, A.; Schneider, E. K.; Weis, P.; Chakraborty, I.; Fuhr, O.; Lebedkin, S.; Parak, W. J.; Kappes, M. M. Linear Size Contraction of Ligand Protected Ag29 Clusters by Substituting AG with Cu. *ACS Nano* **2020**, *14* (11), 15064−15070.
(68) Mahendranath, A.; Mondal, B.; Sugi, K. S.; Pradeep, T. Direct Imaging of Lattice Planes in Atomically Precise Noble Metal Cluster Crystals Using a Conventional Transmission Electron Microscope. *Chem. Commun.* **2022**, *58* (12), 1906−1909.
(69) Sugi, K. S.; Sandra, A. P.; Nonappa; Ghosh, D.; Mohanty, J. S.; Paulthangam Kannan, M.; Sooraj, B. S.; Srikrishnarka, P.; Roy, J.; Dar, W. A.; Pradeep, T. Secondary Ligand-Induced Orthogonal Self-Assembly of Silver Nanoclusters into Superstructures with Enhanced NIR Emission. *Nanoscale* **2023**, *15* (28), 11927−11934.
(70) Plett, C.; Grimme, S. Automated and Efficient Generation of General Molecular Aggregate Structures. *Angew. Chem. Int. Ed.* **2023**, *62* (4), No. e202214477.
(71) Grimme, S.; Bannwarth, C.; Shushkov, P. A Robust and Accurate Tight-Binding Quantum Chemical Method for Structures, Vibrational Frequencies, and Noncovalent Interactions of Large Molecular Systems Parametrized for All Spd-Block Elements (Z = 1−86). *J. Chem. Theory Comput.* **2017**, *13* (5), 1989−2009.
(72) Bannwarth, C.; Ehlert, S.; Grimme, S. GFN2-XTB—An Accurate and Broadly Parametrized Self-Consistent Tight-Binding Quantum Chemical Method with Multipole Electrostatics and Density-Dependent Dispersion Contributions. *J. Chem. Theory Comput.* **2019**, *15* (3), 1652−1671.
(73) Yehliu, K.; Vander Wal, R. L.; Boehman, A. L. Development of an HRTEM Image Analysis Method to Quantify Carbon Nanostructure. *Combust. Flame* **2011**, *158* (9), 1837−1851.
(74) Shim, H. S.; Hurt, R. H.; Yang, N. Y. C. A Methodology for Analysis of 002 Lattice Fringe Images and Its Application to Combustion-Derived Carbons. *Carbon* **2000**, *38* (1), 29−45.
(75) Romaner, L.; Heimel, G.; Ambrosch-Draxl, C.; Zojer, E. The Dielectric Constant of Self-Assembled Monolayers. *Adv. Funct. Mater.* **2008**, *18* (24), 3999−4006.
(76) Martinez, C. R.; Iverson, B. L. Rethinking the Term "Pi-Stacking.". *Chem. Sci.* **2012**, *3* (7), 2191−2201.
(77) Burmistrova, D. A.; Smolyaninov, I. V.; Berberova, N. T. Modern Trends in the Synthesis of Disulfides: From Metal-Containing Catalysts to Nonmaterial Reagents (Review). *Russ. J. Coord. Chem.* **2023**, *49* (S2), S159−S195.
(78) Gaur, R.; Yadav, M.; Gupta, R.; Arora, G.; Rana, P.; Sharma, R. K. Aerobic Oxidation of Thiols to Disulfides by Silver-Based Magnetic Catalyst. *ChemistrySelect* **2018**, *3* (9), 2502−2508.
(79) Niemann, T.; Stange, P.; Strate, A.; Ludwig, R. When Hydrogen Bonding Overcomes Coulomb Repulsion: From Kinetic to Thermodynamic Stability of Cationic Dimers. *Phys. Chem. Chem. Phys.* **2019**, *21*, 8215.
(80) Yang, Y. M.; Yu, H. Z.; Sun, X. H.; Dang, Z. M. Density Functional Theory Calculations on $\overline{S}S$ Bond Dissociation Energies of Disulfides. *J. Phys. Org. Chem.* **2016**, *29* (1), 6−13.
(81) Corma, A.; Ródenas, T.; Sabater, M. J. Aerobic Oxidation of Thiols to Disulfides by Heterogeneous Gold Catalysts. *Chem. Sci.* **2012**, *3* (2), 398−404.

https://doi.org/10.1021/acsnano.6c03086
ACS Nano XXXX, XXX, XXX−XXX